

Coupled axisymmetric finite element model of a hydraulically amplified magnetostrictive actuator for active powertrain mounts

Suryarghya Chakrabarti^a, Marcelo J. Dapino^{b,*}

^a Cummins, Inc., Columbus, IN 47202, USA

^b Department of Mechanical and Aerospace Engineering, The Ohio State University, Columbus, OH 43210, USA

ARTICLE INFO

Article history:

Received 28 January 2012

Received in revised form

11 May 2012

Accepted 12 May 2012

Available online 26 June 2012

Keywords:

Magnetostriction

Terfenol-D

Actuator

Active powertrain mount

Axisymmetric model

ABSTRACT

A coupled axisymmetric finite element model is formulated to describe the dynamic performance of a hydraulically amplified magnetostrictive actuator for active powertrain mounts. The formulation is based on the weak form representations of Maxwell's equations for electromagnetics and Navier's equation for mechanical systems coupled using a nonlinear magnetomechanical constitutive law for terbium–dysprosium–iron (Terfenol-D). Fluid structure interaction is modeled by computing a bulk fluid pressure based on the volumetric deformation of the fluid chamber and coupling the fluid pressure to the structure through traction on the boundaries encompassing the fluid. Seal friction is quantified using the LuGre friction model. The resulting model equations are coded into the commercial finite element package COMSOL, which is used for meshing and global assembly of matrices. Results show that the model accurately describes the dynamic mechanical and electrical responses of the actuator. A parametric study performed using this model reveals that the actuator's unloaded displacement can be improved by up to 140% by doubling the thickness of the fluid chamber components and reducing seal friction to a fourth of its original value. Other parameters such as permeability and conductivity of the permanent magnet and fluid bulk modulus have a minor effect on actuator performance.

© 2012 Elsevier B.V. All rights reserved.

1. Introduction

A magnetostrictive material exhibits coupling between the mechanical and magnetic states. Through this coupling, the material deforms when exposed to magnetic fields and changes its magnetization when stressed. Short response times and high displacement resolution make magnetostrictive materials attractive for sensors and actuators operating at kHz frequencies [1]. One such application is active automotive engine mounts, in which an actuator is employed to control the mount's dynamic stiffness so as to effectively isolate engine vibrations from the chassis.

Active mount actuators must produce approximately ± 1 mm stroke to fully isolate engine vibrations at the idling frequency [2]. Because active-material drivers capable of sufficiently fast dynamic response for mounts (such as piezoelectrics and magnetostrictives) only produce about 0.1% strain, implementation of these materials in an active mount actuator necessitates stroke amplification. Hydraulic amplification [3,4] is attractive as it can generate large mechanical gain in a compact package. The fluid used for amplification can be either the same as the hydromount's fluid [5] or isolated from it [6]. The former design is more attractive for its simplicity while the latter

is more efficient as the displacement of the smart material driver is not degraded by the compliance of the mount. Chakrabarti and Dapino [7] followed the second design principle and combined a magnetostrictive Terfenol-D driver with a sealed hydraulic amplification mechanism. The resulting actuator exhibits superior gain-bandwidth characteristics and less power consumption than a commercial electromagnetic mount actuator used for benchmarking.

Internal friction in fluid seals and fluid-chamber compliance have a significant effect on the performance of smart hydraulically amplified actuators. As a result, linear models considering 100% energy transmission greatly overestimate the performance of these actuators [3,8]. Chakrabarti and Dapino [9] developed a lumped parameter model considering seal friction, nonlinear Terfenol-D material response and compliance of the fluid chamber components to model the dynamic mechanical response of a magneto-hydraulic actuator. Despite the model's value as an analysis tool, it is not suitable for transducer design because fluid chamber compliance and current-field relationships are difficult to accurately quantify in lumped parameter models. A finite element model is more appropriate for design optimization as it can incorporate in greater detail geometry and material constitutive parameters such as elastic modulus, permeability, and electrical conductivity.

Significant effort has been concentrated on developing finite element frameworks for magnetostrictive transducers. Benbouzid [10] presented a 2D bidirectionally coupled magnetostatic model

* Corresponding author.

E-mail address: dapino.1@osu.edu (M.J. Dapino).

with Terfenol-D constitutive behavior incorporated using surface splines. Kannan and Dasgupta [11] formulated a 2D magnetostatic model with bi-directionally coupled magnetomechanical relations, current induced magnetic fields and electromagnetic body forces. Zhou et al. [12] developed a 2D dynamic finite element model of a unimorph actuator with one way magnetomechanical coupling. The one-way coupled 3D model of Kim and Jung [13] describes force due to magnetostriction driving a coupled fluid-structural model for a sonar transducer. Aparicio and Sosa [14] developed a 3D, fully coupled finite element model including dynamic effects along with validation on a simple one-dimensional example. Mudivarthi et al. [15] utilized a fully coupled, magnetostatic formulation to describe stress-induced flux density changes in Galfenol with no current-induced fields. An updated version of the model includes current-induced magnetic fields but not eddy current losses [16]. Evans and Dapino [17] presented a fully coupled dynamic model for 3D magnetostrictive transducers simultaneously incorporating the effects of eddy currents, structural dynamics, and flux leakage on transducer performance.

This paper couples the weak form equations presented by Evans and Dapino [18] with a nonlinear energy-averaged constitutive model for Terfenol-D to describe the response of the magneto-hydraulic mount actuator developed by Chakrabarti and Dapino [7]. In order to exploit the axisymmetric geometry of the device, the equations are reduced to a 2D axisymmetric form. Vector magnetic potential \mathbf{A} and current density \mathbf{J} are reduced to scalars defined in the out-of-plane direction. Fluid pressure in the actuator is computed as a product of the volumetric change of the fluid chamber and the bulk modulus of the fluid. The computed pressure is coupled to the structural model as applied traction on the edges exposed to the fluid. Friction at the o-ring seals is described using the LuGre friction model which describes friction as an interaction force between microscopic bristles present on the sliding surfaces in contact. The complete system of equations is coded into COMSOL (a commercial finite element package) using the weak form application mode. It is then exported as a Matlab script and executed from the Matlab command line. The Terfenol-D constitutive law and the nonlinear time dependent solver are coded up as Matlab functions. Built-in COMSOL functions are called for meshing and global assembly of system matrices.

Section 2 briefly revisits the design of the modeled actuator. Section 3 describes the finite element formulation in detail while

Section 4 discusses the Terfenol-D constitutive law and its implementation. Section 5 describes the time-integration scheme used to solve the nonlinear coupled system. This is followed in Section 6 by a comparison of modeled responses to measurements and a parametric study highlighting the sensitivity of the dynamic performance of the actuator to different design parameters.

2. Actuator design

Fig. 1 shows the actuator's geometry; its main components are a fluid chamber with a large-diameter piston at one end driven by a Terfenol-D rod and a small-diameter driven piston at the other end. The magnetic circuit consists of a permanent magnet to provide magnetic bias, a coil to generate the dynamic fields with Terfenol-D at its core, and iron pieces for flux return. Fig. 2 shows the 2D axisymmetric version used for modeling. Some components like the

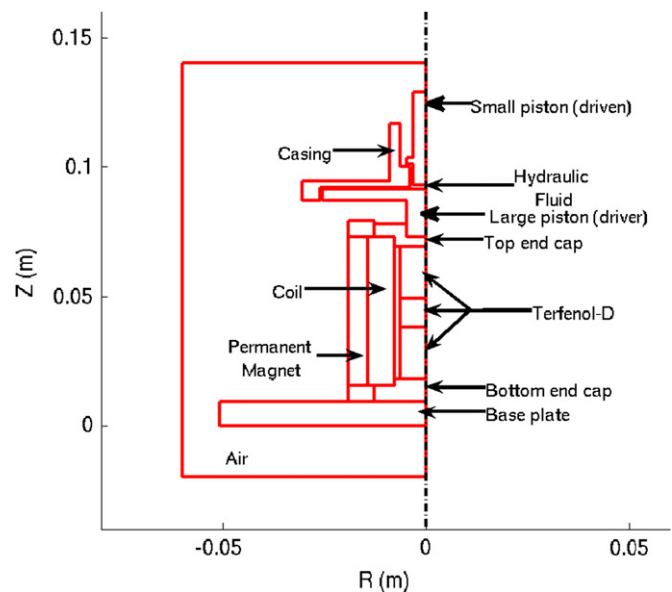


Fig. 2. Geometry of the transducer used in this study.

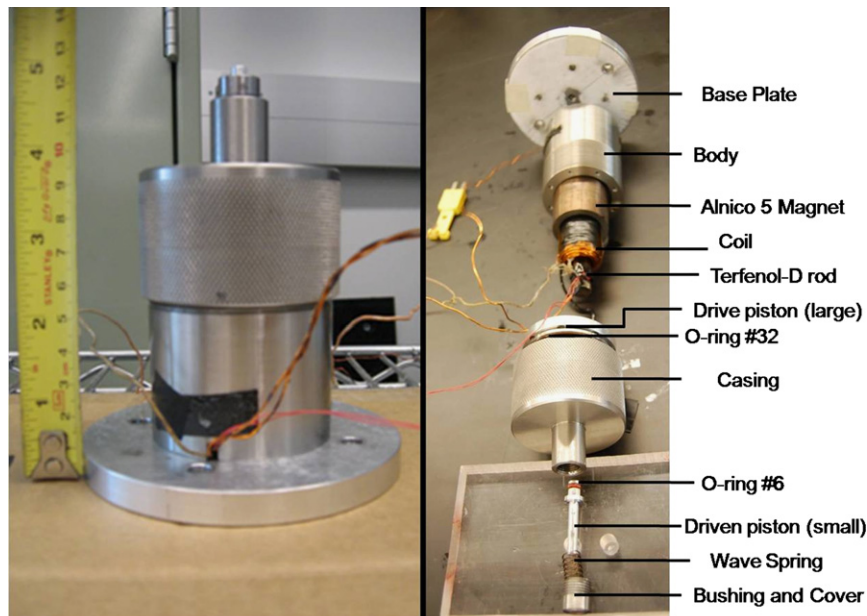


Fig. 1. Assembled and exploded view of the hydraulically amplified magnetostrictive actuator.

stainless steel body and the preload plate have not been modeled as they only serve a geometrical purpose. The device is surrounded by air so that the magnetic potential boundary condition can be applied to the outer boundary of air. In general, flux density measurements are taken by winding a pick-up coil around the middle of the rod and strain measurements are taken by bonding a strain gage close to the midpoint of the rod. Breaking the magnetostrictive rod domain into three areas allows us to evaluate the variables in the central region separately and compare the behavior of the model against measurements. In this actuator all components are considered to be magnetically active, hence the magnetic degree of freedom (\mathbf{A}) is calculated in all the domains. Of these, the base plate, Terfenol-D rod, end caps, pistons, and casing are structurally active, thus the mechanical degrees of freedom \mathbf{u} are calculated only in these components. This partitioning of the solution domain reduces the total degrees of freedom, thus reducing the computation time.

3. Model formulation

3.1. Global relationships and weak form equations

As is the case with many Terfenol-D transducers, the actuator is axisymmetric with the magnetostrictive driver at the core surrounded by a concentric drive coil, permanent magnets, and flux return components. An axisymmetric formulation efficiently describes the actuator without significant loss of accuracy. The current density \mathbf{J} and magnetic potential \mathbf{A} are defined as having only an out-of-plane component (J_ϕ and A_ϕ , denoted as J and A for convenience). To avoid singularities in computation, the variables used in the formulation are the modified magnetic potential ($A' = A/r$), modified radial displacement ($u' = u/r$), and axial displacement (w). The magnetic flux density vector (\mathbf{B}) and the strain vector (\mathbf{S}) are kinematically related to A' , u' , and w by

$$\mathbf{B} = [B_r, B_z]^T = \left[-r \frac{\partial A'}{\partial z}, r \frac{\partial A'}{\partial r} + 2A' \right]^T, \quad (1)$$

$$\mathbf{S} = [S_{rr}, S_{zz}, S_{rz}, S_{\phi\phi}]^T = \left[r \frac{\partial u'}{\partial r} + u', \frac{\partial w}{\partial z}, r \frac{\partial u'}{\partial z} + \frac{\partial w}{\partial r}, u' \right]^T. \quad (2)$$

The corresponding work conjugates magnetic field (\mathbf{H}) and stress (\mathbf{T}) have the form

$$\mathbf{H} = [H_r, H_z]^T, \quad (3)$$

$$\mathbf{T} = [T_{rr}, T_{zz}, T_{\phi\phi}, T_{rz}]^T, \quad (4)$$

and are related to \mathbf{B} and \mathbf{S} through constitutive laws. Since the actuator works primarily under axial loading, the main quantity of interest is the axial deformation w . Thus, w is calculated in all structurally active domains. In the casing and the large piston, radial deformation may occur due to the fluid pressure. Thus, in these two components, radial deformation is also computed. This implies that the casing and the large piston are both axially active and radially active. Domains that are only axially active have a reduced stress and strain vector with only two components, axial and in-plane shear. This reduction significantly simplifies the Terfenol-D constitutive law inversion process. It is emphasized that neglecting the transverse strains does not imply that those strains are zero but rather, they do not contribute to the strain energy density of the material as the corresponding transverse stresses are negligible.

The weak form equations for a generalized magnetostrictive system can be derived from Maxwell's and Navier's equations using the method of weighted residuals [17]. Assuming negligible displacement currents and Lorentz forces, the weak form equations are obtained in terms of the mechanical displacement field \mathbf{u}

and the vector magnetic potential \mathbf{A} :

$$\int_{V_B} \mathbf{H} \cdot \delta \mathbf{B} dV + \int_{V_B} \sigma \frac{\partial \mathbf{A}}{\partial t} \cdot \delta \mathbf{A} dV = \int_{\partial V_B} \mathbf{H}_T \cdot \delta \mathbf{A} d\partial V + \int_{V_B} \mathbf{J}_S \cdot \delta \mathbf{A} dV, \quad (5)$$

$$\begin{aligned} \int_{V_u} \mathbf{T} \cdot \delta \mathbf{S} dV + \int_{V_u} \rho \frac{\partial^2 \mathbf{u}}{\partial t^2} \cdot \delta \mathbf{u} dV + \int_{V_u} \mathbf{c} \frac{\partial \mathbf{u}}{\partial t} \cdot \delta \mathbf{u} dV \\ = \int_{\partial V_u} \mathbf{t} \cdot \delta \mathbf{u} d\partial V + \int_{V_u} \mathbf{f}_B \cdot \delta \mathbf{u} dV. \end{aligned} \quad (6)$$

For an axisymmetric problem the volume integrals can be transformed to area integrals using

$$\int_{V_e} (F) dV = 2\pi \int_{A_e} (rF) dr dz, \quad (7)$$

which when applied to (5) and (6) gives

$$\int_{A_B} r \mathbf{H} \cdot \delta \mathbf{B} dr dz + \int_{A_B} r \sigma \frac{\partial A}{\partial t} \delta A dr dz = \int_{l_B} r H_T \delta A dl + \int_{A_B} r J_S \delta A dr dz, \quad (8)$$

$$\begin{aligned} \int_{A_u} r (\mathbf{T} \cdot \delta \mathbf{S}) dr dz + \int_{A_u} r \rho \frac{\partial^2 \mathbf{u}}{\partial t^2} \cdot \delta \mathbf{u} dr dz + \int_{A_u} r \mathbf{c} \frac{\partial \mathbf{u}}{\partial t} \cdot \delta \mathbf{u} dV \\ = \int_{l_u} r \mathbf{t} \cdot \delta \mathbf{u} dl + \int_{A_u} r \mathbf{f}_B \cdot \delta \mathbf{u} dA. \end{aligned} \quad (9)$$

The weak form equations can be entered in COMSOL using (8) and (9) as a function of A , u , w , and the corresponding test variables even though the solution variables are A' , u' , and w . This is done by adding global expressions relating A and u to A' and u' .

3.2. Fluid domain

Due to the extremely small volume of fluid contained in the actuator, inertial effects in the fluid are neglected. Also, since the seal friction forces are much higher compared to viscous forces in the fluid, damping in the fluid is assumed to be negligible. Thus, only fluid compliance is modeled. The change in volume of the fluid domain ΔV_f can be written as a sum of contributions from the driver piston ΔV_p , the driven piston ΔV_L , and the casing ΔV_C as

$$\Delta V_f = -\Delta V_p + \Delta V_L + \Delta V_C, \quad (10)$$

where each of these volume changes is calculated using the integral

$$\Delta V_i = \int_{l_i} 2\pi r w dr, \quad (11)$$

over the length of the edge l_i exposed to the fluid domain. The pressure change in the fluid is

$$\Delta p = -\frac{\beta}{V_{ref}} \Delta V_f, \quad (12)$$

which is coupled to the structural model through traction on the edges exposed to the fluid. The model describes the effect of compliance of the fluid chamber components. Here, β is the effective bulk modulus of the fluid, while in the lumped parameter model [9], β_{eff} represented an effective modulus describing the combined compliance of the fluid and fluid chamber components.

3.3. Friction model

Friction forces are present at the o-ring seals in the two pistons. At the small (driven) piston seal, actuation forces are low and velocities are high. Hence, even a small friction force at this seal has a significant impact on the dynamic performance of the actuator. On the other hand at the large (drive) piston, actuation forces are high and velocities are low. A small frictional force at this end does not

affect the dynamic response of the actuator. Thus, friction has been modeled only at the small piston seal.

In the LuGre model [19], friction between two sliding surfaces in contact is described as an interaction force between microscopic bristles on both surfaces. The bristle deflection state Z_L is governed by a nonlinear first order differential equation,

$$\dot{Z}_L + \sigma_0 \frac{|v_L|}{g(v_L)} Z_L - v_L = 0, \quad (13)$$

where v_L is the relative sliding velocity between the two surfaces, which in this case is the average velocity of the driven piston calculated by integrating $2\pi r \dot{w}$ over the edge of the piston adjacent to the casing, divided by the area of that surface. Function $g(v_L)$ is given by

$$g(v_L) = F_c + (F_s - F_c) e^{-(v_L/v_s)^2}, \quad (14)$$

where F_s and F_c are the static and Coulomb friction forces and v_s is the Stribeck velocity. The friction force is given by

$$F R_L = \sigma_0 Z_L + \sigma_1 \dot{Z}_L + \sigma_2 v_L, \quad (15)$$

where σ_0 and σ_1 are the bristle stiffness and bristle damping coefficient, respectively. This force is applied as traction on the boundary of the small piston adjacent to the casing.

3.4. Boundary conditions

Boundary conditions for an axisymmetric problem must be implemented such that none of the variables become infinite at the $r=0$ boundary. In this case, the axial symmetry condition is enforced using $(\partial A / \partial r)_{(r=0)} = 0$ in the magnetically active domains, $u_{(r=0)} = 0$ in the radially active domains, and $(\partial w / \partial r)_{(r=0)} = 0$ in the axially active domains. These conditions remove shear stresses and constrain the radial displacement at the $r=0$ boundary. The magnetostrictive system is encapsulated by a large volume of air. At the outer boundaries of this air volume, the magnetic potential is set to zero. The bottom face of the base plate and the casing are considered to be mechanically fixed. The top face of the small piston is spring loaded. Fig. 3 illustrates the boundary conditions used to analyze the actuator.

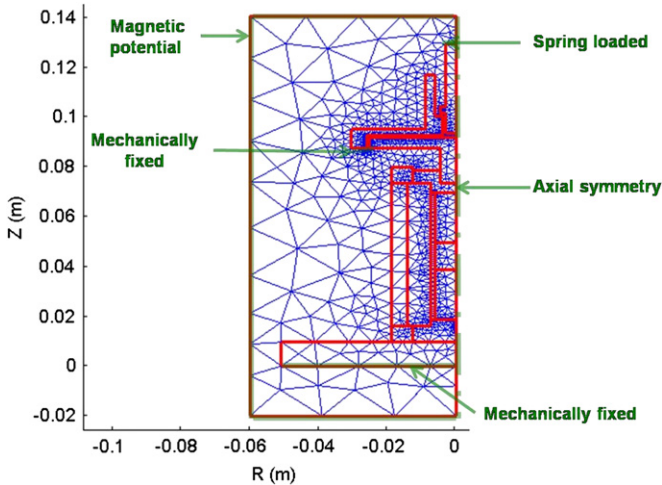


Fig. 3. Mesh and boundary conditions used for finite element analysis of the mount actuator.

4. Constitutive laws

4.1. Terfenol-D constitutive model

Modeling the constitutive behavior of Terfenol-D has been traditionally difficult. The presence of a large magnetostriction anisotropy, low magnetocrystalline anisotropy, and a twinned dendritic structure gives rise to complex domain level processes which are not completely understood [20]. The Jiles–Atherton model [21] quantifies the total magnetization of a ferromagnetic material as the sum of an irreversible component due to domain wall motion and a reversible component due to domain wall bowing. Due to its ease of implementation it has been commonly used to model actuators based on Terfenol-D loaded unidirectionally [22,23]. Another approach to modeling Terfenol-D was formulated by Armstrong et al. [24] where bulk magnetization and magnetostriction are derived from an expected value of a large number of moments. The model was later extended to include magnetomechanical hysteresis and its efficiency was improved by restricting the choice of moment orientations to the easy magnetization axes [25] ($8 \langle 111 \rangle$ directions for Terfenol-D). This restricted choice of moment orientations, however, caused inaccuracies in the models especially in the domain rotation region. Atulasimha et al. [26] improved the accuracy of these models at the cost of increased computational load by tracking the volume fractions of domains aligned along 98 crystallographic orientations for Galfe-nol. Evans and Dapino [18] developed a constitutive model for Galfe-nol by choosing orientations which minimize an energy functional locally defined about each easy axis direction. This eliminated the loss in accuracy in the Armstrong model caused by the restricted choice of moment orientations without adding significant computational burden.

Chakrabarti and Dapino [27] showed that conventional energy averaging with eight easy axis orientations yields an unphysical kink in the magnetization response and fails to describe the gradual approach to saturation present in Terfenol-D magnetostriction. They found that the unphysical kink in the response can be eliminated by superposition of an empirically weighted global anisotropy energy and an anisotropy energy locally defined around each easy axis. The total free energy of a domain close to the k th easy axis \mathbf{c}^k is formulated as the sum of the anisotropy energy G_A^k , magnetomechanical coupling energy G_C^k and the Zeeman energy G_Z^k as

$$G^k = \underbrace{w^k G_{A_0}^k + \frac{1}{2} K^k \|\mathbf{m}^k - \mathbf{c}^k\|^2}_{G_A^k} - \underbrace{\mathbf{S}_m^k \cdot \mathbf{T}}_{G_C^k} - \underbrace{\mu_0 M_s \mathbf{m}^k \cdot \mathbf{H}}_{G_Z^k}, \quad (16)$$

where $G_{A_0}^k$ is the global anisotropy energy and w^k is an empirical weighting factor which adjusts the anisotropy energy along the k th easy axis. Minimization of the energy functional and linearization of a unity norm constraint on the orientation vectors ($\mathbf{m}^k \cdot \mathbf{m}^k = 1 \approx \mathbf{c}^k \cdot \mathbf{m}^k = 1$) yields the following expression for the k th local minimum

$$\mathbf{m}^k = (\mathbf{K}^k)^{-1} \left[\mathbf{B}^k + \frac{1 - \mathbf{c}^k \cdot (\mathbf{K}^k)^{-1} \mathbf{B}^k}{\mathbf{c}^k \cdot (\mathbf{K}^k)^{-1} \mathbf{c}^k} \mathbf{c}^k \right], \quad (17)$$

where the magnetic stiffness matrix \mathbf{K}^k and force vector \mathbf{B}^k are

$$\mathbf{K}^k = \begin{bmatrix} K^k - 3\lambda_{100}T_1 & -3\lambda_{111}T_4 & -3\lambda_{111}T_6 \\ -3\lambda_{111}T_4 & K^k - 3\lambda_{100}T_2 & -3\lambda_{111}T_5 \\ -3\lambda_{111}T_6 & -3\lambda_{111}T_5 & K^k - 3\lambda_{100}T_3 \end{bmatrix}, \quad (18)$$

$$\mathbf{B}^k = [c_1^k K^k + \mu_0 M_s H_1 \quad c_2^k K^k + \mu_0 M_s H_2 \quad c_3^k K^k + \mu_0 M_s H_2]^T. \quad (19)$$

The anhysteretic volume fractions ξ_{an} are calculated using Boltzmann-type averaging,

$$\xi_{an}^k = \frac{\exp(-G^k/\Omega)}{\sum_{j=1}^r \exp(-G^j/\Omega)}, \quad (20)$$

where Ω is an averaging factor defined as a function of the deviation of the anhyseretic domain volume fractions ξ_{an} from a homogeneous distribution $\bar{\xi}$ as

$$\Omega = a_0 + a_1 \|\xi_{an} - \bar{\xi}\|^2. \quad (21)$$

This implicit definition for Ω enables the model to describe the slow approach to saturation in Terfenol-D magnetostriction. However, the implicit relationship demands a suitable iterative solution scheme to converge to consistent values of Ω and ξ_{an} which simultaneously satisfy (20) and (21). Fig. 4 shows the performance of the model in describing measurements presented by Moffett et al. [28].

4.1.1. Model inversion and coordinate transformation

As is common with vector magnetic potential based formulations, a constitutive model inversion is required such that flux density and strain are known inputs, and stress and field are calculated outputs. Moreover, since commercially available Terfenol-D rods have their [112] crystal orientation aligned with the sample axis (which is the Z axis of the global coordinate system), a coordinate transformation is required to integrate the constitutive law with the finite element model. Magnetic flux density and field are first-order tensors and transform according to

$$\mathbf{X}_m = \mathbf{U} \mathbf{X}_G, \quad \mathbf{X}_G = \mathbf{U}^T \mathbf{X}_m, \quad (22)$$

while stress and strain being second-order tensors transform according to

$$\mathbf{X}_m = \mathbf{U}^T \mathbf{X}_G \mathbf{U}, \quad \mathbf{X}_G = \mathbf{U} \mathbf{X}_m \mathbf{U}^T. \quad (23)$$

Here, the subscripts m and G respectively denote the ‘material’ and ‘global’ coordinate system. The transformation matrix \mathbf{U} is formed using the normalized direction vectors in the material coordinate system that are aligned with the global coordinate axes;

$$\mathbf{U} = \begin{bmatrix} \mathbf{u}_R & \mathbf{u}_\phi & \mathbf{u}_Z \\ \|\mathbf{u}_R\| & \|\mathbf{u}_\phi\| & \|\mathbf{u}_Z\| \end{bmatrix}. \quad (24)$$

The direction vector $\mathbf{u}_Z = [112]$; the vectors \mathbf{u}_R and \mathbf{u}_ϕ change with the circumferential angle ϕ . However, since the Terfenol-D driver has an aspect ratio of 4:1, the radial and circumferential components of stresses and fields are expected to be much smaller than the axial components. In that case, considering \mathbf{u}_R and \mathbf{u}_ϕ to be fixed should not have a noticeable effect on the accuracy of the model. In this paper \mathbf{u}_R and \mathbf{u}_ϕ are selected as $[11\bar{1}]$ and $[1\bar{1}0]$ respectively.

Fig. 5 shows a flow chart for the constitutive model. The inputs to the constitutive law are the flux density and strain tensors calculated kinematically from the vector magnetic potential and displacement values at the integration points. The algorithm starts with an initial guess of zero stress and field and converges to the correct values through Quasi-Newton iterations. In every iteration, first the stress and field vectors are transformed from the global to the material coordinate system; then the response of the material to this input stress and field is computed using the energy-averaged constitutive model, and finally the computed flux density $\mathbf{B}_m^{(k)}$ and strain $\mathbf{S}_m^{(k)}$ (k being the iteration index) are transformed back to the global coordinate system ($\mathbf{B}_G^{(k)}, \mathbf{S}_G^{(k)}$) to be compared with the input vectors ($\mathbf{B}_G, \mathbf{S}_G$). In case the difference is greater than the tolerance, a revised stress and field ($\mathbf{H}_G^{(k+1)}$ and $\mathbf{T}_G^{(k+1)}$) is estimated based on the SR1 update formula and the process is repeated until convergence is achieved. The SR1 formula directly approximates the material Jacobian inverse which is used by COMSOL to assemble the tangent stiffness matrix during the dynamic solution process. Since the Terfenol-D rod is considered to be axially active only, a reduced strain vector is fed into the inversion algorithm. The inversion routine forces the radial and circumferential stresses to be zero after each iteration such that the final converged solution at the k th step includes $T_{zz}^{(k)}$ and $T_{rz}^{(k)}$ which yield input strains S_{zz} and S_{rz} along with non-zero values of transverse strains. However, we are only interested in accurately reproducing the axial and in-plane shear components.

4.2. Constitutive laws for passive materials

The stress-strain laws for passive structural materials (such as steel) can be written as shown by Chandrupatla and Belegundu [29]

$$\begin{Bmatrix} T_{rr} \\ T_{zz} \\ T_{\phi\phi} \\ T_{rz} \end{Bmatrix} = \frac{E(1-\nu)}{(1+\nu)(1-2\nu)} \begin{bmatrix} 1 & \frac{\nu}{(1-\nu)} & \frac{\nu}{(1-\nu)} & 0 \\ \frac{\nu}{(1-\nu)} & 1 & \frac{\nu}{(1-\nu)} & 0 \\ \frac{\nu}{(1-\nu)} & \frac{\nu}{(1-\nu)} & 1 & 0 \\ 0 & 0 & 0 & \frac{(1-2\nu)}{2(1-\nu)} \end{bmatrix} \begin{Bmatrix} S_{rr} \\ S_{zz} \\ S_{\phi\phi} \\ S_{rz} \end{Bmatrix}. \quad (25)$$

For domains that are axially active only, the axial stress is computed using the Hooke's law for a uniaxial state of stress, $T_{zz} = ES_{zz}$. The

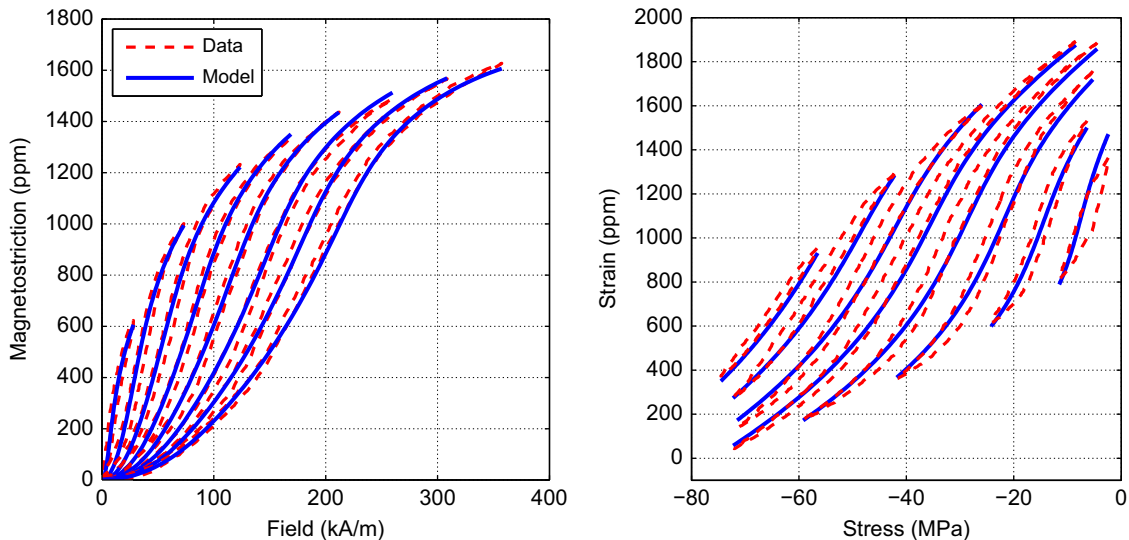


Fig. 4. Comparison of the proposed anhyseretic energy averaged model with measurements by Moffett et al. [28]. All model curves have been generated with the same set of parameters.

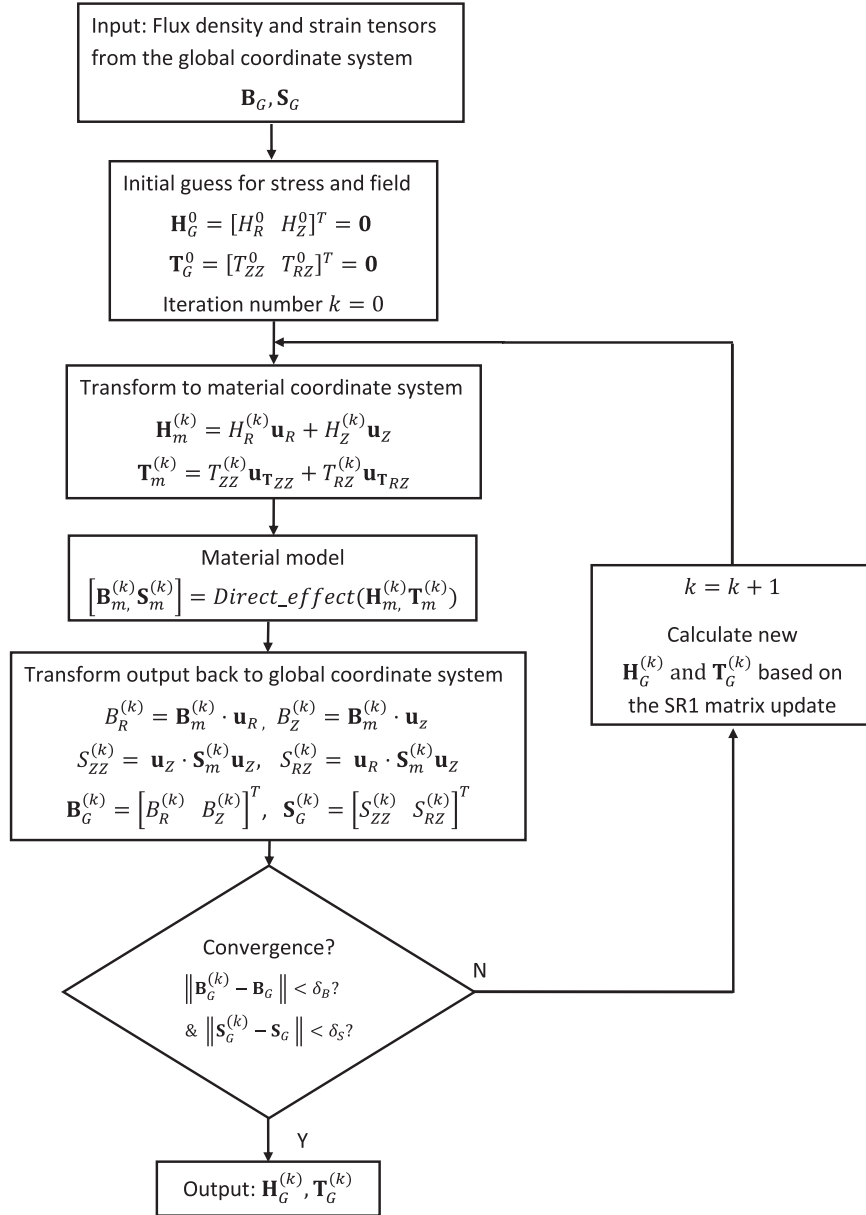


Fig. 5. Flowchart showing the process followed to incorporate the Terfenol-D constitutive law in the model.

shear stress is computed using $T_{rz} = E/[2(1+\nu)]S_{rz}$. Constitutive laws for passive magnetic materials have been modeled using the linear isotropic relationship $\mathbf{H} = \mu^{-1}\mathbf{B}$ where μ is the constant permeability of the material. For permanent magnets this law is modified to include the residual induction B_{res} in the relevant direction. For example, if the residual induction is along the z direction, the constitutive law can be written as

$$H_r = \frac{1}{\mu} B_r, \quad (26)$$

$$H_z = \frac{1}{\mu} (B_z - B_{res}). \quad (27)$$

Electrically conducting materials have been modeled using a constant conductivity.

5. Nonlinear dynamic solution procedure

Solution of nonlinear dynamic systems is a particularly challenging task as even unconditionally stable schemes for linear

systems may become unstable. In this work an implicit time integration scheme is followed based on the trapezoidal rule as described by Bathe [30]. The governing equations for the coupled finite element system can be written as

$$\mathbf{M}\ddot{\mathbf{U}} + \mathbf{D}\dot{\mathbf{U}} = \mathbf{R}(t) - \mathbf{F}(\mathbf{U}, t), \quad (28)$$

where the mass matrix \mathbf{M} , damping matrix \mathbf{D} and state vector \mathbf{U} are of the form

$$\mathbf{M} = \begin{bmatrix} \mathbf{0} & \mathbf{0} \\ \mathbf{0} & \mathbf{M}^u \end{bmatrix}, \quad \mathbf{D} = \begin{bmatrix} \mathbf{D}^A & \mathbf{0} \\ \mathbf{0} & \mathbf{D}^u \end{bmatrix}, \quad \mathbf{U} = \begin{pmatrix} \mathbf{Q}^A \\ \mathbf{Q}^u \end{pmatrix}. \quad (29)$$

The superscripts A and u denote quantities related to the magnetic and mechanical degrees of freedom, respectively. The vector of externally applied forces $\mathbf{R}(t)$ includes contributions from the coil source current density, tangential applied fields, point forces, and traction on certain boundaries. $\mathbf{F}(\mathbf{U}, t)$ is the internal nodal force vector whose derivative with respect to the state vector \mathbf{U} yields the stiffness matrix. Since \mathbf{F} contains contributions from

field and stress which are nonlinearly dependent on \mathbf{U} , the stiffness matrix \mathbf{K} is also state dependent. Bathe [30] suggested various time-integration schemes for nonlinear structural problems of similar form. Explicit methods are ruled out since the mass matrix is singular. An implicit scheme based on the trapezoidal rule is implemented, combined with equilibrium iterations. At the k th iteration the system equations can be written as

$$\mathbf{M}\ddot{\mathbf{U}}^{(k)} + \mathbf{D}\dot{\mathbf{U}}^{(k)} + {}^{t+\Delta t}\mathbf{K}^{(k-1)}\Delta\mathbf{U}^{(k)} = {}^{t+\Delta t}\mathbf{R} - {}^{t+\Delta t}\mathbf{F}^{(k-1)}, \quad (30)$$

$${}^{t+\Delta t}\mathbf{U}^{(k)} = {}^{t+\Delta t}\mathbf{U}^{(k-1)} + \Delta\mathbf{U}^{(k)}. \quad (31)$$

According to the trapezoidal rule of time integration, the following assumptions are used

$${}^{t+\Delta t}\mathbf{U} = {}^t\mathbf{U} + \frac{\Delta t}{2}({}^t\dot{\mathbf{U}} + {}^{t+\Delta t}\dot{\mathbf{U}}), \quad (32)$$

$${}^{t+\Delta t}\dot{\mathbf{U}} = {}^t\dot{\mathbf{U}} + \frac{\Delta t}{2}({}^t\ddot{\mathbf{U}} + {}^{t+\Delta t}\ddot{\mathbf{U}}). \quad (33)$$

The vectors $\ddot{\mathbf{U}}^{(k)}$ and $\dot{\mathbf{U}}^{(k)}$ can be written using (31) to (33) as

$${}^{t+\Delta t}\ddot{\mathbf{U}}^{(k)} = \frac{4}{\Delta t^2}({}^{t+\Delta t}\mathbf{U}^{(k-1)} - {}^t\mathbf{U} + \Delta\mathbf{U}^{(k)}) - \frac{4}{\Delta t}({}^t\dot{\mathbf{U}} - {}^t\ddot{\mathbf{U}}), \quad (34)$$

$${}^{t+\Delta t}\dot{\mathbf{U}}^{(k)} = \frac{2}{\Delta t}({}^{t+\Delta t}\mathbf{U}^{(k-1)} - {}^t\mathbf{U} + \Delta\mathbf{U}^{(k)}) - {}^t\dot{\mathbf{U}}. \quad (35)$$

Substitution in (30) yields the equation of motion for the system;

$$\begin{aligned} & \left[{}^{t+\Delta t}\mathbf{K}^{(k-1)} + \frac{4\mathbf{M}}{\Delta t^2} + \frac{2\mathbf{D}}{\Delta t} \right] \Delta\mathbf{U}^{(k)} \\ &= {}^{t+\Delta t}\mathbf{R} - \mathbf{M} \left[\frac{4}{\Delta t^2}({}^{t+\Delta t}\mathbf{U}^{(k-1)} - {}^t\mathbf{U}) - \frac{4}{\Delta t}({}^t\dot{\mathbf{U}} - {}^t\ddot{\mathbf{U}}) \right] \\ & \quad - \mathbf{D} \left[\frac{2}{\Delta t}({}^{t+\Delta t}\mathbf{U}^{(k-1)} - {}^t\mathbf{U}) - {}^t\dot{\mathbf{U}} \right] - {}^{t+\Delta t}\mathbf{F}^{(k-1)}. \end{aligned} \quad (36)$$

The starting values for the first iteration in a time step are obtained from the values in the final iteration of the previous time step.

$${}^{t+\Delta t}\mathbf{F}^{(0)} = {}^t\mathbf{F}, \quad {}^{t+\Delta t}\mathbf{U}^{(0)} = {}^t\mathbf{U}. \quad (37)$$

The convergence criteria used in this work are based on energy and the norm of the out-of-balance load vector [30]. Mathematically they can be written as

$$\frac{\| {}^{t+\Delta t}\mathbf{R} - {}^{t+\Delta t}\mathbf{F}^{(k-1)} - \mathbf{M}({}^{t+\Delta t}\ddot{\mathbf{U}}^{(k-1)} - {}^t\ddot{\mathbf{U}}) - \mathbf{D}({}^{t+\Delta t}\dot{\mathbf{U}}^{(k-1)} - {}^t\dot{\mathbf{U}}) \|}{RNORM} \leq RTOL, \quad (38)$$

$$\frac{\Delta\mathbf{U}^{(k)} \cdot ({}^{t+\Delta t}\mathbf{R} - {}^{t+\Delta t}\mathbf{F}^{(k-1)} - \mathbf{M}({}^{t+\Delta t}\ddot{\mathbf{U}}^{(k-1)} - {}^t\ddot{\mathbf{U}}) - \mathbf{D}({}^{t+\Delta t}\dot{\mathbf{U}}^{(k-1)} - {}^t\dot{\mathbf{U}}))}{\Delta\mathbf{U}^{(1)} \cdot ({}^{t+\Delta t}\mathbf{R} - {}^t\mathbf{F} - \mathbf{M}({}^t\ddot{\mathbf{U}} - {}^t\ddot{\mathbf{U}}) - \mathbf{D}({}^t\dot{\mathbf{U}} - {}^t\dot{\mathbf{U}}))} \leq ETOL. \quad (39)$$

The mass and damping matrix are state-independent and hence are assembled only once for the entire simulation. The internal nodal force vector \mathbf{F} and the tangential stiffness matrix \mathbf{K} are assembled in every iteration as they are state-dependent. Evaluation of \mathbf{F} requires computation of the total stress and field for a given flux density and strain distribution, for which the Terfenol-D constitutive law is inverted using the Quasi-Newton SR1 formula as discussed in Section 4. The SR1 formula updates the Jacobian inverse directly, eliminating the need for matrix inversion within the iteration loop. Moreover, the approximate Jacobian inverse computed in the final iteration of the inversion process is used for assembling the global stiffness matrix.

Table 1

Parameter values for the fluid and friction models.

Parameter	Value	Description
β/V_{ref}	$12 \times 10^{13} \text{ N/m}^5$	Ratio of bulk modulus to volume of hydraulic fluid
$k_{pre} \text{ (N/m)}$	3.5×10^3	Stiffness of the preload spring
$\sigma_0 \text{ (N/m)}$	0.34×10^5	LuGre bristle stiffness coefficient
$\sigma_1 \text{ (Ns/m)}$	35	LuGre viscous damping coefficient
$\sigma_2 \text{ (Ns/m)}$	5.2	LuGre viscous damping coefficient
$v_s \text{ (m/s)}$	0.0009	Stribeck velocity
$F_c \text{ (N)}$	3.25 (for $v > 0$)	Coloumb friction force for positive relative sliding velocity
	1.75 (for $v < 0$)	Coloumb friction force for negative relative sliding velocity
$F_s \text{ (N)}$	3.25 (for $v > 0$)	Static friction force for positive relative sliding velocity
	1.75 (for $v < 0$)	Static friction force for negative relative sliding velocity

Table 2

Terfenol-D constitutive model parameters.

Parameter	Value	Parameter	Value
$K \times 10^5 \text{ (J/m}^3\text{)}$	4.189	$a_1 \times 10^3 \text{ (J)}$	48.18
$\mu_0 M_s \text{ (T)}$	0.99415	$w^{(1,2)}$	1.147
$\lambda_{100} \times 10^3$	0.104	$w^{(3,4)}$	1.058
$\lambda_{111} \times 10^3$	1.486	$w^{(5,6,7,8)}$	0.958
$a_0 \times 10^3 \text{ (J)}$	3.428	$E_s \text{ (GPa)}$	115

6. Model validation and parametric study

The numerical values of the model parameters were found using analytical, experimental, and empirical procedures. Table 1 lists the parameter values for the fluid and friction models. The preload spring stiffness was measured in a tension–compression machine; the rest of the fluid and friction model parameters were estimated empirically. The LuGre model parameters are within the same order of magnitude as those reported by Canudas de Wit et al. [31].

The constitutive model parameters for Terfenol-D were obtained using a numerical optimization process to describe the magnetomechanical behavior of commercially available Terfenol-D as provided by ETREMA Products [32]. Table 2 lists the Terfenol-D constitutive model parameters.

Finally, the electrical, mechanical and magnetic constitutive parameters for the passive materials are listed in Table 3. This also includes the passive properties of Terfenol-D such as density, conductivity, and structural damping coefficient.

6.1. Obtaining the bias point

To calculate the dynamic response of the actuator, its bias point needs to be accurately determined. The actuator is biased both mechanically and magnetically. The mechanical bias is due to the compression of the wave spring whose force is transmitted (and amplified) through the fluid to the Terfenol-D rod. The stress developed in the Terfenol-D under an axial load can be assumed to be uniform. Therefore, this stress is superimposed directly on the applied stress in the constitutive model. The magnetic bias is due to the residual flux density in the permanent magnet. This field depends on the geometry of the magnetic circuit and cannot be assumed to be homogeneously distributed in the rod. The magnetic bias point is obtained by increasing the residual flux density of the magnet from zero to its actual value using a hyperbolic tangent function and storing the solution from the final step. Fig. 6 shows that the axial magnetic field at the bias

Table 3
Passive material parameters.

Parameter	Description	Air	Al	Cu	Steel	Alnico	Terfenol-D
μ_r	Relative permeability	1	1	1	4e3	5	Model-based
$\sigma \times 10^6$ (S/m)	Electrical conductivity	0	35.8	59.6	5.96	2	1.7
ρ (kg/m ³)	Mass density	NA	2594	NA	7860	NA	7870
ν	Poisson's ratio	NA	0.3	NA	0.3	NA	Model-based
E (GPa)	Young's modulus	NA	70	NA	200	NA	Model-based
c (Ns/m ⁴)	Structural damping	NA	0	NA	1e-2	NA	1×10^{-2}

point is uniformly distributed in the central region of the rod with a somewhat lower value at the ends. The average magnetic field in the Terfenol-D rod is ≈ 30 kA/m.

6.2. Response to harmonic inputs

Fig. 7 shows the actuator response at 20, 50, 100, and 200 Hz. As expected the phase between voltage and displacement increases with increasing frequency resulting in counter-clock-wise rotation of the loops. One shortcoming of the model is the assumed anhysteretic Terfenol-D behavior which causes a discrepancy in the phase of the response. At lower frequencies this is not visible but at 200 Hz the phase difference is significant.

It is observed in both the experimental and modeled voltage-current loops that the actuator draws a biased current even though it is driven with an unbiased sinusoidal voltage input. This happens because of the nonlinear behavior of Terfenol-D. Because the permeability of the material is field dependent, the back emf in the coil also varies with voltage giving rise to an asymmetric current signal. Such effects can only be described accurately with models where electromagnetic and mechanical responses are fully coupled.

6.3. Parametric study

The proposed finite element model can be a useful tool for optimizing device geometry and material selection. To illustrate, the effect on unloaded actuator displacement of fluid bulk modulus, thickness of the fluid chamber components, conductivity and permeability of the permanent magnet, and seal friction force are studied at 20, 50, 100 and 200 Hz.

The effective fluid bulk modulus affects the dynamic performance of hydraulic devices. To investigate the effect of increased fluid stiffness (by degassing), the model is run with $\beta = 2\beta_0$ and $\beta = 4\beta_0$, where β_0 is nominal bulk modulus of the fluid. Fig. 8(a) shows that increasing the bulk modulus four times only leads to a 2–3% increase in unloaded stroke below 100 Hz and a modest 8.5% increase at 200 Hz. This weak dependence suggests that the unloaded displacement is limited by structural compliance and not fluid compliance, which is very low because of the small volume of fluid used in this actuator (≈ 1.3 c.c.).

Next, the effect of structural compliance of the fluid chamber components on transducer performance is investigated. The model is run with the thickness of the large piston and the casing doubled. A 30–35% stroke increase is calculated in the 20–100 Hz range while a 143% increase is obtained at 200 Hz. Thus, the primary sources of compliance in the transducer are the components enclosing the fluid.

Another factor that influences the performance of hydraulic devices is seal friction. The friction force at the small piston seal is reduced to $f_r = 0.5 f_{r0}$ and $f_r = 0.25 f_{r0}$, where f_{r0} is the nominal friction force. With the friction force reduced by a half, the stroke increases by 10–12% in the 20–100 Hz range while a 60% increase is calculated at 200 Hz. With the friction force reduced to one fourth of the original value, a 15–20% stroke increase is calculated below

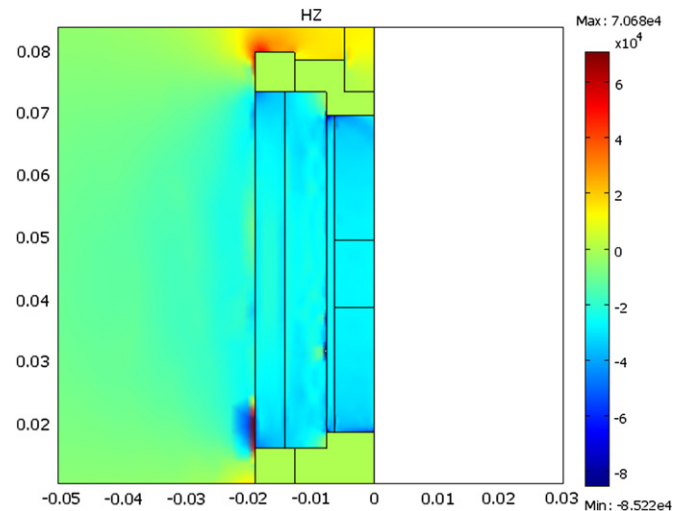


Fig. 6. Axial magnetic field distribution in the magnetic circuit due to the permanent magnet.

100 Hz and an 85% increase is calculated at 200 Hz. As expected, reduction in seal friction can create considerable improvements in the unloaded stroke of the transducer.

Finally, to illustrate the advantages of a fully coupled model, the effect of key electromagnetic parameters on the mechanical performance of the actuator is studied. The permeability of the permanent magnet is increased to twice and four times the initial value while the conductivity of the permanent magnet is reduced to zero to study the effect of eliminating eddy currents on the permanent magnet. Neither parameter has an appreciable effect on system performance. Increasing the permeability of the permanent magnet four times leads to a 4% stroke increase at 20 Hz and reduces to a 0.25% increase at 200 Hz. Setting the conductivity of the permanent magnet to zero results in negligible improvement at 20 Hz and gradually increases up to a 3.6% stroke improvement at 200 Hz. These trends are expected because an increase in magnetic permeability leads to a larger total flux in the circuit. However, increased flux also results in higher eddy currents as the drive frequency increases. Thus the advantage of a higher permeability diminishes with increasing drive frequency. Conversely, reducing the conductivity of the permanent magnet has little effect at 20 Hz since eddy currents are negligible at low frequencies. With increasing frequency the effect of reduced eddy currents becomes more apparent (Fig. 8(b)).

7. Concluding remarks

This paper presents a coupled axisymmetric finite element model of a Terfenol-D mount actuator. Maxwell's equations and Navier's equations are coupled through a nonlinear magnetomechanical constitutive law for Terfenol-D. The effects of eddy currents, flux leakage, structural dynamics, fluid compliance, fluid-structure

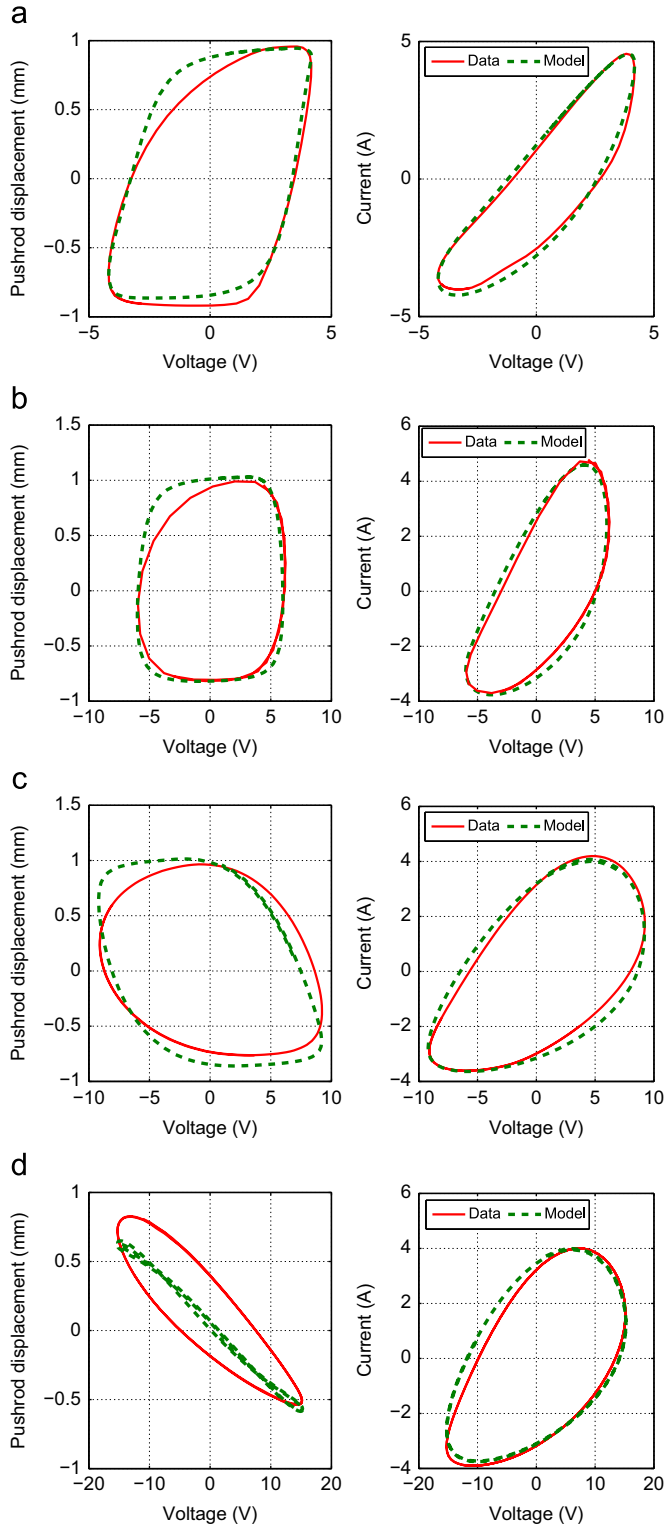


Fig. 7. Comparison of modeled voltage–displacement and voltage–current loops with measurements at (a) 20 Hz, (b) 50 Hz, (c) 100 Hz, (d) 200 Hz.

interaction, and nonlinear constitutive behavior are simultaneously incorporated. This makes the model capable of accurately describing the dynamic mechanical and electrical behavior of the actuator. At high frequencies the model shows discrepancies in the phase of the output due to the assumed anhysteretic Terfenol-D constitutive law. A parametric study on the unloaded displacement response of the actuator shows that significant performance improvements can be

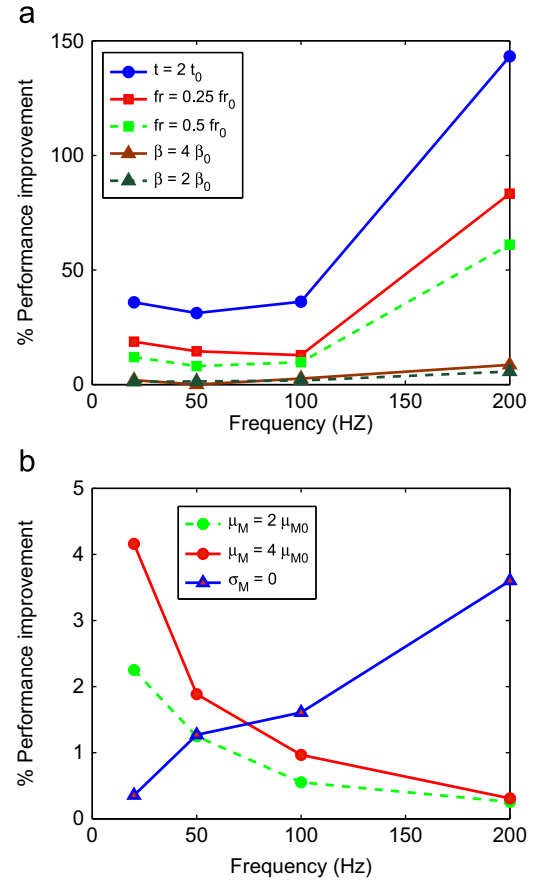


Fig. 8. Percentage improvement in the unloaded stroke of the actuator with variation in: (a) mechanical model parameters and (b) magnetic model parameters.

achieved by stiffening the structural components enclosing the fluid chamber and reducing seal friction. It is also found that the actuator's performance is not very sensitive to changes in fluid bulk modulus due to the extremely small fluid volume contained in the hydraulic chamber. Variation of the electrical and magnetic constitutive parameters (permeability and conductivity) of the permanent magnet creates no appreciable improvements in transducer performance. However, the example illustrates the utility of the fully coupled modeling framework in describing the effects of electrical and magnetic constitutive parameters on the mechanical performance of the transducer.

Acknowledgments

Financial support for this research was provided by the member organizations of the Smart Vehicle Concepts Center, a National Science Foundation Industry/University Cooperative Research Center (www.SmartVehicleCenter.org), the National Science Foundation through Grant #IIP-0732517, and ONR MURI Grant # N000140610530 (Jan Lindberg program manager).

References

- [1] M. Dapino, On magnetostrictive materials and their use in adaptive structures, *Struct. Eng. Mech.* 17 (3–4) (2004) 303–329.
- [2] Y. Lee, C. Lee, Dynamic analysis and control of an active engine mount system, *Proc. Inst. Mech. Engrs D J. Auto. Eng.* 216 (2002) 921–931.
- [3] H.-S. Yoon, G. Washington, P. Eyabi, M. Radhamohan, S. Woodard, R. Dayton, A millimeter-stroke piezoelectric hybrid actuator using hydraulic displacement amplification mechanism, in: *IEEE International Symposium on Industrial Electronics*, vol. 4, July 2006, pp. 2809–2813.

- [4] V. Giurgiutiu, C. Rogers, R. Rusovici, Solid-state actuation of rotor blade servo-flap for active vibration control, *J. Intel. Mater. Syst. Struct.* 7 (2) (1996) 192–202.
- [5] T. Ushijima, S. Kumakawa, Active engine mount with piezo-actuator for vibration control, *SAE* (930201).
- [6] T. Shibayama, K. Ito, T. Gami, T. Oku, Z. Nakajima, A. Ichikawa, Active engine mount for a large amplitude of engine vibration, *SAE* (951298).
- [7] S. Chakrabarti, M.J. Dapino, Hydraulically amplified terfenol-d actuator for adaptive powertrain mounts, *ASME J. Vib. Acoust.* 133 (2011) 61015.
- [8] J. Garcia-Bonito, M. Brennan, S. Elliott, A. David, R. Pinnington, A novel high-displacement piezoelectric actuator for active vibration control, *Smart Mater. Struct.* 7 (1) (1998) 31–42.
- [9] S. Chakrabarti, M. Dapino, A dynamic model for a displacement amplified magnetostrictive driver for active mounts, *Smart Mater. Struct.* 19 (2010) 055009.
- [10] M.E.H. Benbouzid, R. Beguenane, G. Reyne, G. Meunier, Finite element modeling of Terfenol-D magneto-mechanical coupling: application to a direct micro-stepping rotary motor, in: *IEEE International. Electric Machines and Drives Conference Record*, 1997, pp. WC2/6.1–WC2/6.3, 1997.
- [11] K. Kannan, A. Dasgupta, A nonlinear Galerkin finite-element theory for modeling magnetostrictive smart structures, *Smart Mater. Struct.* 6 (1997) 341–350.
- [12] H. Zhou, Y. Zhou, Vibration suppression of laminated composite beams using actuators of giant magnetostrictive materials, *Smart Mater. Struct.* 16 (2007) 198–206.
- [13] J. Kim, E. Jung, Finite element analysis for acoustic characteristics of a magnetostrictive transducer, *Smart Mater. Struct.* 14 (2005) 1273–1280.
- [14] J. Pérez-Aparicio, H. Sosa, A continuum three-dimensional, fully coupled, dynamic, non-linear finite element formulation for magnetostrictive materials, *Smart Mater. Struct.* 13 (2004) 493–502.
- [15] C. Mudivarthi, S. Datta, J. Atulasimha, A. Flatau, A bidirectionally coupled magnetoelastic model and its validation using a galferol unimorph sensor, *Smart Mater. Struct.* 17 (2008).
- [16] F. Graham, C. Mudivarthi, S. Datta, A. Flatau, Modeling of a Galferol transducer using the bidirectionally coupled magnetoelastic model, *Smart Mater. Struct.* 18 (2009) 104013.
- [17] P. Evans, M. Dapino, Dynamic model for 3-D magnetostrictive transducers, *IEEE Trans. Magn.* 47 (1) (2011) 221–230.
- [18] P.G. Evans, M.J. Dapino, Efficient magnetic hysteresis model for field and stress application in magnetostrictive galferol, *J. Appl. Phys.* 107 (6) (2010) 063906.
- [19] H. Olsson, K.J. Astrom, C.C. de Wit, M. Gafvert, P. Lischinsky, Friction models and friction compensation, *Eur. J. Control* 4 (3) (1998) 176–195.
- [20] Y. Huang, Y. Jin, Phase field modeling of magnetization processes in growth twinned Terfenol-D crystals, *Appl. Phys. Lett.* 93 (2008) 142504.
- [21] D. Jiles, D. Atherton, Theory of ferromagnetic hysteresis, *J. Magn. Magn. Mater.* 61 (1–2) (1986) 48–60.
- [22] M. Dapino, R. Smith, A. Flatau, Structural magnetic strain model for magnetostrictive transducers, *IEEE Trans. Magn.* 36 (May) (2000) 545–556.
- [23] W. Huang, B. Wang, S. Cao, Y. Sun, L. Weng, H. Chen, Dynamic strain model with eddy current effects for giant magnetostrictive transducer, *IEEE Trans. Magn.* 43 (April) (2007) 1381–1384.
- [24] W. Armstrong, Magnetization and magnetostriction processes in $\text{tb}_{0.27}\text{—}0.30\text{dy}_{0.73}\text{—}0.70\text{fe}_{1.9}\text{—}2.0$, *J. Appl. Phys.* 81 (5) (1997) 2321–2326.
- [25] W.D. Armstrong, An incremental theory of magneto-elastic hysteresis in pseudo-cubic ferro-magnetostrictive alloys, *J. Magn. Magn. Mater.* 263 (2003) 208.
- [26] J. Atulasimha, G. Akhras, A. Flatau, Comprehensive 3-d hysteretic magneto-mechanical model and its validation with experimental single-crystal iron-gallium behavior, *J. Appl. Phys.* 103 (2008) 07–336.
- [27] S. Chakrabarti, M.J. Dapino, Fully coupled discrete energy-averaged model for terfenol-d, *J. Appl. Phys.* 111 (5) (2012) 054505.
- [28] M. Moffett, A. Clark, M. Wun-Fogle, J. Linberg, J. Teter, E. McLaughlin, Characterization of Terfenol-D for magnetostrictive transducers, *J. Acoust. Soc. Am.* 89 (1991) 1448.
- [29] T. Chandrupatla, A. Belegundu, *Introduction to Finite Elements in Engineering*, 3rd ed., Prentice-Hall, Upper Saddle River, New Jersey 07458, 2002.
- [30] K. Bathe, *Finite Element Procedures*, Prentice Hall, Upper Saddle River, New Jersey 07458, 1996.
- [31] C. Canudas de Wit, H. Olsson, K. Astrom, P. Lischinsky, A new model for control of systems with friction, *IEEE Trans. Autom. Control* 40 (3) (1995) 419–425.
- [32] Etrema Products Inc., Terfenol-D Data Sheet.